Research Square

Preprints are preliminary reports that have not undergone peer review.
They should not be considered conclusive, used to inform clinical practice,
or referenced by the media as validated information.

CD19-CAR-T phenotyping during Prodigy manufacturing uncovers critical T cell transition

Florian Schinle

florian.schinle@web.de

University Childrens Hospital Tuebingen

Florian Schinle

University Childrens Hospital Tuebingen https://orcid.org/0009-0006-6053-9608

Isa-Maria Klink

University Childrens Hospital Tuebingen

Felix Schäfer

NMI Natural and Medical Sciences Institute at the University of Tuebingen

Sylvia Klein

University Childrens Hospital Tuebingen

Katrin Lutz

University Childrens Hospital Tuebingen

Maximilian Feige

University Childrens Hospital Tuebingen

Kathrin Wolsing

University Childrens Hospital Tuebingen

Simon Fink

NMI Natural and Medical Sciences Institute at the University of Tübingen https://orcid.org/0000-0001-7460-8201

Tamam Bakchoul

University Hospital of Tuebingen https://orcid.org/0000-0002-6797-6812

Claudia Lengerke

University Hospital Tuebingen https://orcid.org/0000-0001-5442-2805

Karin Schilbach

Childrens Hospital University of Tuebingen https://orcid.org/0000-0001-8041-055X

Peter Lang

Children's University Hospital https://orcid.org/0000-0001-7737-2142

Markus Templin

NMI Natural and Medical Sciences Institute at the University of Tuebingen https://orcid.org/0000-0002-6569-6489

Christian Seitz

University Childrens Hospital Tuebingen

Daniel Atar

University Children's Hospital Tuebingen

Article

Keywords:

Posted Date: March 23rd, 2026

DOI: https://doi.org/10.21203/rs.3.rs-9071948/v1

License: This work is licensed under a Creative Commons Attribution 4.0 International License.
Read Full License

Additional Declarations: There is **NO** Competing Interest.

Abstract

Advances in cell therapy engineering have driven chimeric antigen receptor T cell manufacturing from manual procedures to highly automated and technically sophisticated production systems. To meet the increasing demand for high-throughput manufacturing, current efforts focus on accelerating production while maintaining/increasing product quality. Yet, to date, the precise daily progression of the T cell states during manufacturing have not been examined in detail.

Here we characterize anti-CD19 CAR-T cell manufacturing on a CliniMACS Prodigy platform under current good manufacturing practice (cGMP) conditions, integrating cytotoxic activity profiling with comprehensive phenotyping across a complete production cycle. Using over 130 extra- and intracellular markers related to T cell activation, CAR signaling, metabolism, apoptosis, and hypoxia, we identify a pivotal transition point between process days 5 and 7 marking the shift from early activation to a stable/durable, functionally more specific T cell phenotype.

These data shed light on cellular remodeling throughout semi-automated CAR-T manufacturing and provide a mechanistic framework for modulating T cell phenotypes across distinct production phases.

Introduction

A decade after their clinical debut, chimeric antigen receptor (CAR)-T cells continue to redefine the limits of engineered immunity, revealing both unprecedented therapeutic durability and a complex landscape of resistance that now shapes the field’s most urgent research questions. The CAR is a chimeric molecule of a T cell receptor (TCR) fused with an antigen recognition domain, such as a single-chain fragment (scFv) of a monoclonal antibody [1-4]. This approach enables long-term disease control and offers the additional advantage of rapid onset of action [5, 6]. Building on their remarkable clinical successes, ranging from durable remissions in refractory B-cell malignancies to expanding indications in myeloma and beyond, CAR-T therapies now face a pivotal bottleneck in manufacturing, where the biological constraints of T cell activation meet the practical realities of scalable production [7, 8].

An outstanding question is how the inherently artificial process of CAR-T cell manufacturing affects the functional properties and phenotypic characteristics of the generated cells. From a metabolic perspective, the manufacturing process dramatically diverges from physiological T cell expansion. When cultivated in standard medium (Iscove's modified Dulbecco medium), cells receive 25 mM glucose and 4 mM glutamine. Without knowing the exact amounts in TexMACS, it can be assumed that the values are also significantly higher than physiological levels. T cells cultivated in cell culture medium (TexMACS™) are then exposed to 5-times times the standard blood sugar level, 8-times the standard glutamine level, and two to four times the oxygen partial pressure compared to the conditions in the blood [9]. Additionally, these cells undergo supraphysiological activation via CD3/CD28 stimulation and are exposed to cytokine concentrations (IL-7 and IL-15) that far exceed physiological levels [10]. These additives primarily aim to enhance longevity, proliferative capacity, and antitumor efficacy of the final CAR-T cell product, thereby promoting increased stemness [11, 12]. CAR-T cell products enriched with a

high proportion of stem cell memory (TSCM), naïve (TN), or central memory (TCM) T cells exhibit superior antitumor responses and in vivo persistence [13]. However, conventional protocols require extended ex vivo culture periods (7 to 14 days) resulting in the reduction/depletion of some of these subsets [14].

Shortened processes are promising approaches to increase stemness and there are already some trends in this direction [14, 15]. In these studies, cell pools at the midpoint of cell culture (day 5), where characterized by the enrichment of TSCM and TCM. In contrast, prolonged culture (day 10) resulted in a more terminally differentiated phenotype dominated by terminal effector function cells (TEFF) [16]. Furthermore, approaches of 24-hour processes seem to preserve a significantly higher percentage of naive and stem cell-like T cells eliminating the ex vivo expansion step [14]. There is a prevailing assumption that increased speed is inherently beneficial. However, the exact temporal ordering of events and a full combinatorial analysis of changes to the phenotype, metabolism, and functionality of the cells have remained largely unexplored. Accordingly, the potential gains and compromises inherent to early CAR-T cells remain unresolved.

In this study, we dissect the molecular chronology of a GMP-compliant anti-CD19 CAR-T cell manufacturing process by interrogating each individual day, rather than an abbreviated process. Using an in vitro tumor re-challenging model we investigated potential cellular triggers and markers of senescence and exhaustion through multicolor flow cytometry and DigiWest™-based phosphoproteomic profiling (>130 surface/intracellular markers). This comprehensive approach illuminates T cell activation trajectories, CAR-T signaling dynamics during/after tumor engagement and the underlying metabolic/stress adaptions. Critically we define key inflection points that govern phenotypic trade-offs between rapid cytolytic potency and sustained effector durability, offering actionable control points for bespoke CAR-T engineering.

Results

Standardized GMP manufacturing and structured in-process sampling design

Three CliniMACS Prodigy® manufacturing runs were performed. Prodigy 1 and Prodigy 2 were initiated with apheresis collections from distinct donors as biological replicates. Bystander cells were depleted through T cell enrichment using CD4- and CD8-labeled magnetic beads. Following enrichment, cultures were initiated at a density of 1 x10^8 CD4+/CD8+ cells/mL in 100 mL culture volume. A technical replicate for Prodigy 2 was generated by allocating excess cells on day 0 resulting in Prodigy 2A and Prodigy 2B. A defined sampling scheme was chosen to capture the entire manufacturing process, while minimizing volume depletion from any single run (Fig. 1 A). All subsequent steps, such as T cell activation using Miltenyi TransAct™ reagent, were executed independently on each device.

Paired analysis between Prodigy 1 and Prodigy 2A for viable cell concentration, cell specific growth rate and cell size were performed using a two-sided paired t test and revealed no significant differences (p >

0.05, Supplementary Table 1). Under the tightly controlled cGMP conditions, combined with the statistical analysis between runs, the replicates were considered highly comparable and were therefore pooled for subsequent data analyses.

Early and late manufacturing stages yield functionally distinct CAR-T cytotoxic profiles

A luciferase-expressing Burkitt's lymphoma (Raji) cell line was used as the CD19-CAR target. This line has been widely employed as a benchmark model for CD19-CAR responsiveness in previous studies [10, 17, 18]. Raji cells underwent three sequential rounds of co-culture with CAR-T cells (tumor contacts, TC 1 – TC 3) at a fixed effector to target (E:T) ratio of 4:1. To prevent carryover of soluble factors between challenges, culture supernatant was removed prior to each re-stimulation. Flow cytometry analysis of Raji cells confirmed that incomplete lysis between rounds did not result in substantial transfer of viable tumor cells with fewer than 1 % of Raji cells traceable at TC 3 (Supplementary Figure 1). Cytotoxicity assays across a range of E:T ratios (4:1, 2:1, 1:1, 1:2, 1:4, 1:8, 1:16 and 1:32) were performed before the first and after each subsequent tumor contact.

In addition, a cytotoxicity assay was performed on a CD19 knock-out Raji cell line (CD19KO) to determine non-specific cytotoxic activity. Cytotox data (Fig. 2 A) of samples taken directly from the CliniMACS Prodigy® (referred to as TC 0) showed a significant negative correlation between increasing process days and tumor cell lysis after 72 hours of incubation with CAR-T cells at E:T 1:1 (Fig. 2 B and Supplementary Table 2). Additional evaluation of E:T 1:4 and 4:1 can be found in Supplementary Figure 2. Process days closer to harvest (day 6 to 12) did not reach 100 % cell lysis making them less potent than early cells. On Raji CD19 KO, CAR-T cells showed a similar negative trend, but were significantly lower than TC 0 (Supplementary Table 3). Thereby showing specificity towards the target antigen. Contrary to these observations, CAR-T cells that had encountered tumor cells in three cycles (TC 3), showed a positive correlation between increasing process days a tumor cell lysis, showing more durability. To evaluate the effect of the effector cell count and its capacity for proliferation, cell specific growth rate was analyzed between each TC (48 hours). Additional data was collected for cells cultivated in medium without tumor cells (RPMI) prior to TC 1 (Fig. 2 C). The cell specific growth rate decreased significantly in later process days (Supplementary Table 4). However, the negative slope was flattening with increasing tumor cycles (TC 2 to TC 3). Interestingly, in samples of harvest day 12, the cell specific growth rates in all TCs were close to 0. CD4+ to CD8+ ratios were examined via flow cytometry analysis (Fig. 2 D). Towards harvest day 12, the ratio was favoring CD8+ cells for both TC 0 and TC 3. No CAR expression was observed on day 0 due to lentiviral transduction on process day 1. CAR-expression could be detected by day 2. The proportion of CAR+ cells reached a peak on day 6, followed by a slight decline towards day 12. In samples taken after TC 3, the proportion of CAR+ cells steadily increased in correlation with increasing process days.

Manufacturing stage–dependent dynamics shape CAR-T activation profiles

Both extracellular and intracellular data were examined to capture T cell activation dynamics continuously over the course of the process. Extracellular activation marker expression was evaluated

via flow cytometry of CD4+ or CD8+ cells expressing CD25 and/or CD69 (Fig. 3 A). A high content of early (CD25-/CD69+) and robustly activated (CD25+/CD69+) cells was found on day 2. We expected an increased abundance of early-activated cells on day 1, however, due to the transduction process no sample could be taken. A predominance of cells in late activation (CD25+/CD69-) was found between day 4 and 6. At process day 12, cells almost exclusively comprised inactive cells (CD25-/CD69-).

Evaluation of T cell activation at the intracellular level, was evaluated by DigiWest™ analysis [19]. Normalization to process sample day 0 (respective for Prodigy 1 and Prodigy 2) was chosen for all analytes of T cell activation. Markers and their phosphorylations, involved early in the activation cascade were found with reduced signals on process days 2 to 5 (Fig. 3 B). Across the 12-day process, markers CD3ε, CD8α, Lck, Ras, phosphorylation of LAT at tyrosine-191 and PLCγ1 showed a distinct biphasic pattern with a critical transition between day 5 and 7, a period coinciding with the described pattern described by flow cytometry. Further downstream, markers such as JNK2, ERK1/2, mTOR, NFκB1 and NFκB p65, exhibited a lasting reduction from day 2 up until day 12 (Fig. 3 C).

Tumour-induced CAR-signaling profiles

Following TC 3, a high proportion of inactive cells was detected in early process samples, particularly prominently among CD8+ cells (Fig. 4 A). In contrast, harvest day 12, activated cells constituted the majority of the population. In comparison to Fig. 3 A, these findings suggest effective reactivation of CAR-T cells after repeated tumor contact. Proteins such as ZAP-70, ASK1, or ERK1, key components of the initial signaling hub downstream (Fig. 4 D) of the of T cell receptor [20-22] as well as CAR signaling [28-30], displayed activated forms, though upregulation or phosphorylation between day 3 to 5, prior to tumor contact/engagement (Supplementary Figure 4). The signals for c-Jun, a core component of the AP-1 transcription factor complex and thus a critical regulator of proliferation under stress conditions [31], showed a distinctly phase-dependent pattern throughout the process (Fig. 4 C). Unlike the aforementioned upstream proteins, c-Jun activation was strongly reflected in TC 3 samples, showing a strong signal early in the process and an attenuation towards the end of the process.

Transient stress and exhaustion-related signatures characterize early expansion phase

Flow cytometry analyses were performed employing markers LAG-3, PD-1 and TIM-3 (Fig. 5 A). LAG-3 expression for Prodigy 1 was consistently low. Prodigy 2, showed an increase in expression between day 2 and day 8, then a decline towards day 12 (TC 0). In TC 3 both Prodigy 1 and Prodigy 2 displayed a transient increase in LAG-3 expression before declining. Prodigy 2 showed a decreasing curve, while Prodigy 1, being at a lower level, increased towards day 8. PD-1-expression was aligned among Prodigy 1 and Prodigy 2. TC 0 showed a peak between days 2 and 3 for both CD4+ and CD8+ cells. In TC 3 for CD4+ cells, PD-1 showed an initial peak at day 3 and a subsequent second peak on day 7, subsequently falling again. For CD8+ cells, values remained consistently low. TIM-3-expression rose sharply for both CD4+ and CD8+ cells between days 2 and 3 (TC 0). The expression remained relatively stable, with singular variations between Prodigy 1 and Prodigy 2 on individual days. On day 12, Prodigy 1 had significantly lower TIM-3 expression compared to Prodigy 2. For CD4+ cells in TC 3, TIM-3 showed a

similar expression pattern to PD-1. In contrast, CD8+ cells of TC 3 showed two peaks of high TIM-3 expression on day 3 and on day 7.

Intracellularly, the Caspase 3 (35 kDa) inactive form [32] remained stable between day 0 and 3, increased moderately from day 4 onwards, reflecting the renewed availability of the proenzyme (Fig. 5 B Apoptosis). At TC 3, the inactive form was present in low levels, with negative peaks for both day 0 and 3. Activated 19 kDa Caspase 3 [32] displayed a short-lived yet pronounced peak (days 2 to 4) in TC 0 and then returned to baseline levels. While in TC 3, this form was constantly elevated. The Caspase 3-generated 89 kDa cleavage product PARP [33] diverged between Prodigy 1 and 2, with a steep reduction on day 4 up to day 12 for Prodigy 2. While in Prodigy 1, levels sank from day 2 to 6 and then elevated again to 12. Its uncleaved form (116 kDa) shows two peaks on day 0 and between day 6 and 7. Both Bim isoforms (15 kDa and 23 kDa) have a strictly proapoptotic effect [34]. Bim showed early activation induction (day 2 to 3), followed by a reduced signal, consistent with an acute proapoptotic stress response that is dampened again after initial T cell activation. In TC 3, both isoforms showed a low signal until day 3, followed by a continuous increase until day 12. Bcl2, the key anti-apoptotic antagonist of Bim [34], showed reduced signal intensity by day 4, returning to baseline level by day 12, indicating an early attenuation of survival signaling during the activation phase followed by late re-stabilization.

In TC 3, Bcl2 showed a pronounced negative trend (Fig. 5 B Apoptosis). Survivin, a key protein for proliferation and mitotic stability [35], was strongly elevated until day 4 and then dropped significantly. In TC 3, Survivin remained largely constant, suggesting subdued proliferative reactivation in the tumor context. The protein p53, with pro- and anti-apoptotic influence [36], increased until day 4 and then declined. Its phosphorylation at serine-37 was low until day 3, but then showed a marked increase until day 8. After repetitive tumor contact, p53 phosphorylation peaked between days 4 and 6.

Analytes Lactate dehydrogenase A (LDHA), Hypoxia-inducible factor 1 (HIF1), Carboanhydrase IX (CA IX), and Forkhead box protein O3 (FoxO3a) were selected to assess hypoxia during CliniMACS Prodigy® manufacturing (Fig. 5 B Hypoxia). LDHA plays a key role in energy production through the metabolism of lactate to pyruvate and vice versa [37]. LDHA showed a strong early increase of approximately two log2-steps between day 0 and day 2. HIF1α is a protein unit that controls cellular response in low oxygen conditions. It is part of the transcription factor HIF-1, which stabilizes in the cell nucleus during oxygen deficiency and activates genes together with another subunit HIF1β (ARNT) [38]. Both peaks overlapped between day 2 and 6. Data on HIF1 were available exclusively for Prodigy 2. CA IX, a canonical HIF1 target and pH regulator in tumor cells [39], initially declined in signal strength from day 0 to day 2. The signal then returned to baseline levels by day 4, followed by another decline and subsequent continuous increase until day 12. The phosphorylation of FoxO3a at Serine-318/321, key marker of FoxO3a inactivation [40], decreased by approximately three log2 steps between day 0 and day 5. This strong dephosphorylation event indicated functional reactivation and potential nuclear translocation. Subsequently, phosphorylation increased, peaking on day 7, followed by a decrease until

day 12. The opposing regulation of total protein and phosphorylation signal underscored the relevance of its posttranslational control.

Metabolic activity was examined by several key players. A limiting transporter for glucose-dependent energy supply GLUT-1 [41] showed an abrupt increase of four log-2 levels between day 0 to day 2, indicating early, massive upregulation of glucose uptake after cell activation (Fig. 5 B Metabolism). This was followed by a slight further increase until day 5, followed by stabilization, reflecting a transition from the initial activation phase to a metabolically established state. Hexokinase I, which is responsible for the first irreversible glycolysis reaction [42], showed an early decline on day 2, suggesting a temporary reduction in basal glycolysis flux. From day 4 onward, a continuous re-induction was observed until initial levels were restored on day 12. Hexokinase II exhibited a pronounced increase between day 0 and day 2, indicating early metabolic reprogramming. A peak on day 3 pointed to the phase of maximum glycolytic induction, followed by a slight decline until day 5, as is typical during transitions from acute activation to stabilized metabolic states. A renewed slight increase until day 12 suggests persistent or renewed metabolic demands, possibly in the course of continued expansion. PKM2, the pyruvate kinase isoform, typical of proliferating and activated cells [43], showed a temporal course that closely correlated with the pattern of Hexokinase II. This underscored the coordinated upregulation of two central enzymes of glycolysis during metabolic reprogramming. Between day 0 and day 2, there was a marked increase, suggesting an early enhancement of glycolytic throughput. The moderate decline until day 5, followed by a slight increase again until day 12. AMPKα phosphorylation at threonine-172 indicates its activated form as a mediator for metabolism of lipids [44]. It highlighted a pronounced decline between day 0 and day 2, indicating an early phase of metabolic relief or sufficient energy reserves. Subsequently, phosphorylation increased strongly until day 5.

Discussion

Semi-automated CAR-T cell manufacturing is a huge step forward in decentralized point-of-care manufacturing. Several strategies for processes shortening have already been proposed [10, 14, 45, 46]. The present study characterizes manufacturing on the CliniMACS Prodigy®, delineating distinct phenotypic phases, and highlighting options for process optimization and rational process shortening.

Cytotoxic anti-tumor activity reveals temporal shift

To identify critical shifts during manufacturing, a combination of complementary high-resolution analytical approaches was employed. A cytotox-re-challenge model served as an analytical approach for functionality of CAR-T cells, which allowed for canonical sampling of all essential process days (Fig. 6).

First tumor encounter revealed a significant negative temporal correlation. Complete tumor cell lysis (E:T at 1:1) was only detected in samples collected in earlier days of the manufacturing process (early potency). It has been reported that early CARs induced non-specific lysis, indicative of NKG2D-mediated, target-independent tumor cell killing [47, 48], however, tumor lysis in our study was significantly lower in the controls where targets were CD19 negative. This suggests, enhanced early tumor lysis cannot be

explained by activation alone; and that CAR function already contributes early, driving superior efficacy versus day 12. This means that the CAR is responsible for the early high lytic activity. Interestingly, following repeated tumor contact, samples from early process phases exhibited markedly poorer lysis than those from late phases, despite reduced proliferative capacity late phase cells exhibited increased durability. This day-dependent reversal of functional properties prompted comprehensive profiling of activation state, metabolic programs and overall phenotype to delineate the timing and mechanistic basis of this shift.

CD4/CD8 ratio during manufacturing

To identify the reasons for the dramatic loss of tumorolytic activity during CAR manufacturing, we also analyzed the CD4/CD8 ratio. A conspisious observation was a shift of the CD4:CD8 ratio, favoring $CD8^+$ cells in the later process day samples, a trend that has also been described in other studies on CliniMACS Prodigy® cultivation [46, 49, 50]. A shift that has been accounted for supportive influence of CD4+ T cells on CD8+ T cell expansion [51] or might result from fundamentally different biology of CD4+ T cells vs CD8+ T cells regarding proliferation and cell division. Although both CD4+ and CD8+ T cells undergo an autonomous program of differentiation, the kinetics and efficiency of CD8+ T cell proliferation differ substantially from those of CD4+ T cell proliferation. The time of antigen exposure required to launch the proliferative program for naive CD8+ T cells seems to be less than that required for naive CD4+ T cells [52-55]. CD8+ T cells also divide sooner and have a faster rate of cell division than do CD4+ T cells [51, 52, 56-58]. For clinical translation a 1:1 CD4:CD8 T cell ratio is favored, preclinical and clinical data show that a balanced mix promotes expansion in patients and persistent antitumor activity [59]. However, retrospective analysis of clinical data has shown that a higher proportion of CD8+ cells is beneficial for the clinical outcome, with higher response rates [60]. Consequently, the observed $CD8^+$ dominance appears to be a direct result of the inherent proliferative advantage of this subset, posing a structural challenge for maintaining a strictly balanced 1:1 ratio during extended automated manufacturing.

T cell Activation State

Following T cell enrichment, cells were activated using polymers targeting both CD3 and CD28 in the presence of cytokines. Upon recognition of antigen–MHC complexes, the TCR–CD3 complex underwent rapid internalization (Supplementary Figure 7) followed by swift degradation [61-63]. Flow cytometry data confirmed robust activation of both CD4+ and CD8+ cells 48 hours post stimulation with over half exhibiting late state activation markers, a pattern consistent with prior resports [64]. This late-activated fraction remained predominant in both subsets until day 6 after which an inactive phenotype progressively emerged with CD8+ cells showing faster exhaustion by day 12. Notably, TCR-proximal signaling proteins (e.g. Lck, PLCγ, PKCθ, RAS) displayed biphasic dynamics (Fig. 3), featuring early depletion and re-expression to baseline by days 5–6, most pronounced for Lck, a key regulator of TCR signaling and trafficking [65, 66]. In contrast nuclear and transcriptional effectors (e.g. JNK2, ERK1/2,

mTOR, NF-κB1, NF-κB p65) [20, 21, 24], showed profound, sustained depletion through day 12, except for c-Jun, which peaked sharply on day 2 before declining, as typical for immediate-early genes [67].

Compared to the endogenous TCR, CAR-T cell stimulation yields different functional outcomes in sensitivity, effector function, and exhaustion. CAR and TCR form separate immunological synapses without direct cross-phosphorylation of their CD3ζ chains [68] with CAR triggering faster cytotoxicity and IFN-γ release [68, 69] but reduced proliferative capacity upon prolonged exposure [70, 71]. At the molecular level, CAR induces weaker LAT phosphorylation than TCR [72] (Supplementary Figure 8) rendering TCR up to 100 times more antigen-sensitive [72]. While TCR-driven activation efficiently generates potent effector cells [71], these are short-lived due to activation-induced cell death (AICD) [73]. Here, transient CD3/CD28 hyperactivation upregulated PD-1 by day 4 post tumor-contact, curbing late stage effector function in re-challenge assays. Surviving cells, acting as a selective filter, transitioned into a durable, long-lived pool. Subset analysis further revealed an early TEM predominance (days 2–3) a transient TCM peak (days 4–5), followed by sustained CD8+ cells dominance and TCM reaquisition in CD4+ cells (see Suppementary Figure 9). Upon tumor engagement TEM cells overwhelmingly prevailed (with minor TEFF) while TCM remained as a small, transient fraction (days 2–5).

These findings substantially advance our understanding of the observed tumorolytic activity. Incorporating more quiescent yet pre-selected cells at late manufacturing stages ensures sustained cytotoxicity. Conversely, early-stage cells characterized by heightened proliferation and full activation exhibit superior cytolytic potency but diminished durability.

Metabolic reprogramming during CAR-T differentiation

The CAR T manufacturing process demands precise control of multiple parameters to yield sufficient numbers of activated CAR-T cells. The Prodigy system handling high cell densities, particularly late in culture, necessitates frequent medium exchanges. This environment profoundly impacts cellular metabolism, stress responses, and apoptosis – unexplored aspects systematically profiled here.

Post-activation (days 0–2), GLUT-1 exhibited the most pronounced upregulation among all analytes examined, reflecting robust glucose (and hexose/pentose) import critical for metabolic rewiring in the early phase of the manufacturing process. Hexokinase II surged steeply by day 2, peaked on day 3, then plateaued, while PKM2, the dominant glycolytic isoform in proliferating immune cells, mirrored this trajectory [43]. AMPKα – amongst other important metabolic pathways controlling lipid metabolism through phosphorylation [44] rose sharply from day 2, plateauing by day 5 to signal waning activation and lipid metabolism restraint via phosphorylation; this aligned precisely with the proliferation curve.

Through their multifunctional activities, c-myc and mTOR serve as key regulators of cellular metabolic programs. c-myc acts as the primary switch for metabolic reprogramming after antigen recognition [74]. A major function of c-myc in T cells is to control the expression of amino acid transporters [75]. Without c-myc, T cells cannot increase their biomass because they lack the building blocks for protein production [75]. In addition, it controls glutamine metabolism, which is essential for the production of nucleotides

and polyamines [74]. Furthermore, c-myc induces genes for glucose metabolism to provide energy and intermediates for cell growth [74]. mTOR acts as a central integrator of environmental signals, linking nutrient availability to immune functions [76]. The subunit mTORC1 promotes aerobic glycolysis (Warburg effect) and protein biosynthesis [77]. High activity leads to the formation of potent effector cells but prevents the development of memory cells [77]. While mTORC1 drives glycolysis, its inhibition promotes fatty acid oxidation and mitochondrial capacity, which supports the survival of long-term memory cells [77].

Collectively, these findings indicate that metabolic rewiring drives a shift from a purely proliferative toward a specialized effector phenotype. This confirms that the observed transition in cytotoxic activity is fundamentally rooted in the cells' changing energetic and biosynthetic requirements across different manufacturing stages.

LDHA upregulation confirms glycolytic adaptation under hypoxia

Additionally, cellular stress responses were evaluated with particular emphasis on hypoxia. Under hypoxic or anaerobic conditions, lactate dehydrogenase A (LDHA) preferentially converts pyruvate to lactate, thereby regenerating NAD+ from NADH to maintain glycolytic flux [37].

LDHA upregulation is hypoxia-inducible via HIF-1α, enhancing lactate production in low-oxygen environments typical of tumors or inflamed tissues. This maintains glycolytic flux when oxidative phosphorylation is limited. LDHA signals peaked between days 3 and 5, preceding daily media changes and indicating hypoxia. More definitively, HIF-1α, continuously synthesized and degraded under normoxia – stabilizes under low oxygen, accumulates in the cytoplasm, translocates to the nucleus. dimerizes with HIF1ß for an active transcription factor which drives hypoxic gene transcription [38]. HIF1α peaked between days 2 and 4, followed by elevated HIF-1β levels on days 4 and 8. Carbonic anhydrase IX (CA IX) a canonical HIF-1 target, localizes on the cell surface under hypoxia where it regulates extracellular pH through electrolyte secretion and acid-base homeostasis and was detected by days 4–6 [39]. These temporal synchronized dynamics, alongside LDHA upregulation confirm transient hypoxic conditions during the middle phase of the process (days 4 to 6).

FoxO3a which serves as a key transcription factor that senses and responds to diverse cellular stresses such as oxidative damage, nutrient deprivation, and hypoxia [78], further supports this mid-phase stress response. FoxO3a declined sharply by day 5, peaked thereafter and fell again by day 12, its inhibitory phosphorylation at Ser318/321 followed an comparable, more amplified pattern [79].

Daily media exchange starts on day 5, coinciding with peaks of hypoxia markers like LDHA/HIF-1α, followed shortly thereafter by the expression of exhaustion markers post-tumor contact (Fig. 5 A), suggesting cumulative O_2 depletion mid-culture. However, some stress-related responses such as LAG-3 expression and FoxO3a phosphorylation varied across biological replicates (Fig. 5 A and B), implying some donor-specific T cell sensitivity to transient hypoxia rather than a uniform process flaw. While the early rise of hypoxia markers suggests that an earlier initiation of media exchanges could mitigate

metabolic stress, such an intervention requires a careful trade-off. It might prolong the proliferative phase, it also risks diluting essential autocrine cytokines and bypassing the “natural selection” that yields a more robust and mature cell product. Consequently, this transient hypoxic stress likely acts as a key physiological trigger that drives the observed shift toward a less proliferative, yet more durable T cell phenotype.

Apoptosis, Proliferation Marker and anti-Apoptotic Dynamics

To integrate these findings on a specific type of stress, markers of apoptosis were assessed to determine whether the above-conditions promoted a proapoptotic state. The 35 kDa full length Caspase 3 increased markedly from day 4 onwards, consistent with proenzyme accumulation. In contrast, the activated 19 kDa Caspase 3 displayed a brief but pronounced peak between days 2 and 4 and remained persistently elevated after tumor contact. The 89 kDa PARP cleavage product generated by Caspase 3 declined sharply from day 4 supporting sustained caspase activity. p53 whose predominant biologic function is pro-apoptotic, was upregulated between days 3 and 7 with strong phosphorylation at serine-37 from days 4 and 8, indicating robust p53 activation and severe cellular stress, typically linked to DNA damage [80]. After tumor contact, p53 phosphorylation peaked on days 4 - 6 and on day 12. Both Bim isoforms (15 kDa and 23 kDa), strictly pro-apoptotic, showed dynamically distinct peaks on days 2 - 3, before declining, reflecting acute stress post activation. After tumor contact, Bim rebounded strongly from day 5 onwards.

Bcl-2, Bim`s key antagonist, decreased by day 4, hit a nadir on day 5, but reached its baseline value by day 12. In tumor coculture TC 3, it showed a sustained negative trend. Survivin, essential in mitosis, peaked on days 3 - 5, typical of early proliferative expansion, before normalizing but remained stable in TC 3, indicating blunted proliferation upon tumor engagement. proliferative reactivation in the tumor context.

In contrast to a terminal pro-apoptotic shift, the observed dynamics of Bcl-2, Survivin, and Caspase-3 suggest a transient phase of cellular stress mid-manufacturing that is successfully resolved. Ultimately, the 12-day process yields a product that closely resembles the initial cellular state in terms of viability, rather than showing signs of accumulated apoptotic damage.

Summary

The manufacturing process resolves into distinct early and late phases (Supplementary Fig. 10) demarcated by a critical functional and metabolic inflection point. Shortened protocols generate a phenotype distinct from the standard 12-day process, featuring rapid tumor lysis but compromised persistence (Fig. 6). Conversely, late-stage cells display delayed yet more specific and durable effector function.

Unexpectedly, exhaustion markers were enriched in early samples, owing to hyperacute initial activation, whereas day 12 cells exhibited metabolic profiles resembling a naïve-like state, aligning with recent

observations from CliniMACS Prodigy® processes [50]. While abbreviated manufacturing accelerates therapy delivery [14, 16], our data reveal associated phenotypic trade-offs in yield and quality that can be strategically exploited: fast-acting, high-yield profiles for aggressive tumors versus the sustained specificity of late-stage cells for minimal residual disease.

Methods

CAR-T Manufacturing

CliniMACS Prodigy® TS 520 (200073-613), CliniMACS® PBS/EDTA Buffer CR/GMP (200070-022), TexMACS™ GMP Medium (170076-306), MACS® GMP Recombinant Human IL-7 (170076-111), MACS® GMP Recombinant Human IL-15 (170076-186), CliniMACS® CD4 Reagent CR/GMP (200070-213), CliniMACS® CD8 Reagent CR/GMP (200070-215) and MACS® GMP T Cell TransAct™ Large Scale CR/GMP (200076-204) were derived from Miltenyi Biotec. Bags were placed in the right position for waste, target, non-target and formulation. Leak-test and priming were initiated. Starting material was welded to the application bag and the content was then transferred into it. Vials of CD4 and CD8 MicroBeads were spiked to the system. T cell enrichment and automated red blood count reduction were initiated. After determining concentration of CD4+/8+ cells, adjustment to cell count of 1 $x10^8$ cells in 100 mL were done by CliniMACS Prodigy®, after entering the data. Finally, activation of T cells was started after spike of TransAct™. 24 hours after activation, viral transduction was performed, a CD19-CAR Lentivirus bag (Miltenyi Biotec, 200-072-102), was thawed at RT. The bag was then welded to the tube set. Transduction was initiated on the system. Cultivation volume was increased to 200 mL on day 3 and remained constant. Medium exchange of 50 mL on day 5 and 130 mL was performed every day starting day 6 and two-times a day from process day 9 on. Cultivation was done until day 12. Samples were collected for day 0, between day 2 to 8 and harvest day 12.

Cytotoxic Assay

Luciferase-transduced Raji cells (DSMZ, ACC 319) had been previously transduced with luciferase gene in our lab [81]. The tumor cell lines were seeded at a density of 30,000 cells per well in 50 µL complete RPMI medium in a flat white 96-well cell culture plate (Greiner Bio-One, 655083). Dissolved D-luciferin potassium salt (PerkinElmer, 122799-5) was added to each well at a concentration of 4 µg/mL. Effector cells were seeded at the specified effector-target cell ratios (E:T). The total volume per well was 200 µl. The plates were incubated in a HERAcell incubator (Heraeus Med, 98111578) at 37 °C and 5% CO_2. Bioluminescence was measured with the Tecan Spark 10M (Tecan, 189000545) at 37 °C at the specified time points. Lysis was calculated based on the relative luminescence of the test conditions using a lysis formula based on a standard dilution series.

Re-Challenge

Raji cells (DSMZ, ACC 319) were seeded at 0.5 $x10^6$ cells per well in 1 mL complete RPMI in 6-well cell culture plates. 2 $x10^6$ effector cells in 2 mL of complete RPMI. The cells were incubated in a HERAcell

incubator (Heraeus Med, 98111578) for 48 hours at 37 °C and 5 % CO2.

Flow Cytometry Analysis

Anti-human antibodies used include: CD3 Antibody, anti-human, Vio® Bright R720 (Miltenyi Biotec, 130-127-377), CD4-VioGreen® (Miltenyi Biotec, 130-113-259), CD8-PE (Miltenyi Biotec, 130-110-678), CD19-APC (Miltenyi Biotec, 130-113-642), CD25-Vio® Bright B515 (Miltenyi Biotec, 130-115-536), CD27-BUV496 (BD OptiBuild™, 741145), CD45RA-VioBlue® (Miltenyi Biotec, 130-117-743), CD45RO-APC-Vio® 770 (Miltenyi Biotec, 130-113-557), CD69-Brilliant Violet 650™ (BioLegend, 310933), CD95 Antibody BUV737-Anti-Human (BD Horizon™, 612790), CD279 (PD1)-APC (Miltenyi Biotec, 130-120-389), CD223 (LAG-3)-BV786 (BD OptiBuild™, 744727) and CD366 (TIM-3)-PE-Vio® 770 (Miltenyi Biotec, 130-121-334).

0.3 x 10^6 cells were prepared in 3 mL cold CliniMACS® PBS/EDTA buffer (Miltenyi Biotec, 200-070-025) in a round-bottom centrifuge tube. After washing, cells were prepared with FcR Blocking Reagent, human (Miltenyi Biotec, 130-059-901) at 0.6 µL 300 µL of cell suspension, followed by incubation for 10 minutes at 4 °C. After second wash, antibodies were added with two panels (Panel 1: CD3, CD4, CD8, CD27, CD19-CAR Biotin, CD45RA, CD45RO, CD25, CD69, CD95 and Panel 2: CD3, CD4, CD8, CD27, CD19-CAR Biotin, PD-1, TIM-3, LAG-3) and incubated for 30 minutes at 4 °C. Followed by washing and secondary anti-biotin antibody staining with incubation for 30 minutes at 4 °C (Panel 1:Biotin-APC and Panel 2: Biotin-FITC). Final 7-AAD live-dead staining was performed. Cells were processed on a FACS Fortessa X-20 (BD Biosciences, H656385J4001).

Intracellular Analysis

The DigiWest™ approach is a bead-based Western blot method that enables highly parallel analysis of protein expression and modification status with molecular weight resolution [19]. For each sample, 2 x10^6 cells were collected and centrifuged at 450 x g for 5 minutes at 4 °C in a 50 mL low-bind centrifuge tube (Eppendorf, 0030122240). The supernatant was aspirated carefully. The pellet was then resuspended in 5 mL cold 1x DPBS, the suspension was transferred to a new 50 mL low-bind centrifuge tube. Cells were spun down again at 450 x g for 5 minutes at 4 °C, the supernatant was again aspirated carefully. This step was repeated one more time. The dry pellet was then snap-frozen on dry ice and stored at -80 °C.

Samples were lysed with 50 µL lysis buffer (2% LDS, 25mM DTT, PhosSTOPTM Phosphatase Inhibitor, cOmpleteTM Protease Inhibitor) for 20 minutes at 95 °C. Then spun 5 minutes at 16,000 x g in a QIAshredder (Quiagen, 79656) column. Proteins were separated by size using SDS-polyacrylamide gel electrophoresis (SDS-PAGE), transferred to a membrane, and biotinylated. The sample lane was cut into 96 horizontal strips representing molecular weight fractions, and the proteins are eluted. The eluted proteins were then immobilized on neutravidin-coated Luminex beads, with each of the 96 bead sets representing a defined molecular weight fraction. The pooled beads, which now correspond to a digitized Western blot trace, were incubated with specific antibodies in the immunoassay and the signals are read out using a Flexmap 3D instrument (Luminex Corp. Austin, TX). Intrinsic marker proteins were used to

accurately assign the molecular weight to the 96 bead populations. Quantitative evaluation was performed by an algorithm that visualizes the protein bands as peaks and integrates their area above a local baseline, yielding numerical output values.

Statistical information

Unless otherwise stated, the individual values were represented in each plot. The number of independent experiments and the total number of repetitions (n) are indicated in the respective figure description. Analytical replicates (n = 3) done in cytotoxic assays are represented by their mean values.

Normality was tested prior to linear regression analyses two-tailed paired t-tests using a Shapiro-Wilk test.

Paired comparisons between Prodigy 1 and Prodigy 2A for viable cell concentration, cell specific growth rate and cell size were analyzed using a two-sided paired t test. The number of paired observations (n) was 5 (process day 2, 4, 6, 8 and 12). Data are presented as the mean paired difference (Prodigy 2A – Prodigy 1) together with the 95% confidence interval (CI). The assumptions of normality were assessed on the paired differences using the Shapiro–Wilk test. Test statistics (t and degrees of freedom) and exact P values are reported in Supplementary Table 1. A p value < 0.05 was considered statistically significant.

To analyze unspecific lysis, the same type of t test was applied, with n = 14 paired comparisons. The assumptions of normality were assessed on the paired differences using the Shapiro–Wilk test.

To examine whether process day predicts cytotoxicity, a simple linear regression was performed, with time as the independent variable and cytotoxicity as the dependent variable. The strength and significance of the relationship were assessed using the regression slope, its 95% confidence interval, and the coefficient of determination (R^2). All tests were two-sided with $\alpha = 0.05$.

Statistical analyses were conducted in GraphPad Prism software (version 10.1.1, GraphPad Software, Inc., USA).

Two-dimensional hierarchical clustering (analyte x samples) was performed using MultiExperiment Viewer (MeV) v4.9. Prior to clustering, the data were median-centered and log2-transformed per analyte to make different signal strengths comparable. Distances were calculated using Euclidean distance; clustering was performed agglomeratively with complete linkage. Leaf order optimization was done for improved visualization for analytes and samples.

Declarations

Data Availability

The datasets generated and/or analysed during the current study are available from the corresponding author on reasonable request. For original data, please contact florian.schinle@med.uni-tuebingen.de.

Data Availability

The datasets generated and/or analysed during the current study are available from the corresponding author on reasonable request. For original data, please contact florian.schinle@med.uni-tuebingen.de.

Acknowledgements (optional)

The authors thank all members of the Seitz lab for excellent discussions. Furthermore, we thank the Förderverein für krebskranke Kinder Tübingen e.V. for its support. And finally we want to thank Hans-Dieter Steibl of Miltenyi for his technical support.

Ethics declarations

Competing interests

The authors declare no competing financial interests.

Contributions

F.H.S. and D.A. conceived and designed the study. F.H.S., I.K., F.S., S.F. and M.F. established assay models and panel designs. F.H.S. and I.K. performed the experiments with the assistance of S.K., K.L. and K.W. F.S. performed the DigiWest analysis. Data collection and analysis was done by F.H.S., I.K. and F.S.. F.H.S. and F.R. performed the statistical analyses. Figures were generated by F.H.S.. F.H.S., D.A. and K.S contributed to writing of the manuscript. D.A., C.M.S., M.F.T., T.B., C.L. and P.L. provided scientific oversight. D.A., C.M.S., M.F.T. and P.L. supervised the study.

Corresponding author

Correspondence to: Florian Schinle (ORCID ID: 0009-0006-6053-9608)

Ethics

Only apheresis from healthy donors was used as the starting material for production. This was approved.by the Ethics Committee of the University Hospital Tübingen (ethics approval No. 507/2017B01)

References

1. June, C.H., et al., *CAR T cell immunotherapy for human cancer.* Science, 2018. **359**(6382): p. 1361–1365.

2. Labanieh, L., R.G. Majzner, and C.L. Mackall, *Programming CAR-T cells to kill cancer.* Nature biomedical engineering, 2018. **2**(6): p. 377–391.
3. Rafiq, S., C.S. Hackett, and R.J. Brentjens, *Engineering strategies to overcome the current roadblocks in CAR T cell therapy.* Nature reviews Clinical oncology, 2020. **17**(3): p. 147–167.
4. Rossi, M. and E. Breman, *Engineering strategies to safely drive CAR T-cells into the future.* Frontiers in immunology, 2024. **15**: p. 1411393.
5. Cappell, K.M. and J.N. Kochenderfer, *Long-term outcomes following CAR T cell therapy: what we know so far.* Nature reviews Clinical oncology, 2023. **20**(6): p. 359–371.
6. Mueller, K.P., J.M. Grenier, and E.W. Weber, *CAR T cell persistence in cancer.* Trends in Cancer, 2025.
7. Abou-el-Enein, M., et al., *Scalable manufacturing of CAR T cells for cancer immunotherapy.* Blood cancer discovery, 2021. **2**(5): p. 408–422.
8. Ayala Ceja, M., et al., *CAR-T cell manufacturing: Major process parameters and next-generation strategies.* Journal of Experimental Medicine, 2024. **221**(2): p. e20230903.
9. McNamee, E.N., et al., *Hypoxia and hypoxia-inducible factors as regulators of T cell development, differentiation, and function.* Immunologic research, 2013. **55**: p. 58–70.
10. Jackson, Z., et al., *Automated manufacture of autologous CD19 CAR-T cells for treatment of non-Hodgkin lymphoma.* Frontiers in immunology, 2020. **11**: p. 1941.
11. Tantalo, D.G., et al., *Understanding T cell phenotype for the design of effective chimeric antigen receptor T cell therapies.* Journal for ImmunoTherapy of Cancer, 2021. **9**(5): p. e002555.
12. Cieri, N., et al., *IL-7 and IL-15 instruct the generation of human memory stem T cells from naive precursors.* Blood, The Journal of the American Society of Hematology, 2013. **121**(4): p. 573–584.
13. Rial Saborido, J., et al., *Role of CAR T cell metabolism for therapeutic efficacy.* Cancers, 2022. **14**(21): p. 5442.
14. Ahmadi, M., et al., *Accelerating CAR T cell manufacturing with an automated next-day process.* Current Research in Translational Medicine, 2025. **73**(1): p. 103489.
15. Chen, S. and D. Liu, *Rapid manufacturing of CAR-T therapy: strategies and impact.* Trends in Biotechnology, 2025. **43**(4): p. 745–748.
16. Cadinanos-Garai, A., et al., *High-dimensional temporal mapping of CAR T cells reveals phenotypic and functional remodeling during manufacturing.* Molecular Therapy, 2025. **33**(5): p. 2291–2309.
17. Xiao, Q. and X. Su, *Anti-tumor Efficacy of CD19 CAR-T in a Raji B Cell Xenografted Mouse Model.* Bio-protocol, 2023. **13**(8): p. e4655.
18. Maschan, M., et al., *Multiple site place-of-care manufactured anti-CD19 CAR-T cells induce high remission rates in B-cell malignancy patients.* Nature communications, 2021. **12**(1): p. 7200.
19. Treindl, F., et al., *A bead-based western for high-throughput cellular signal transduction analyses.* Nature communications, 2016. **7**(1): p. 12852.
20. Shah, K., et al., *T cell receptor (TCR) signaling in health and disease.* Signal transduction and targeted therapy, 2021. **6**(1): p. 412.

21. Bhattacharyya, N.D. and C.G. Feng, *Regulation of T helper cell fate by TCR signal strength.* Frontiers in immunology, 2020. **11**: p. 624.
22. Hwang, J.-R., et al., *Recent insights of T cell receptor-mediated signaling pathways for T cell activation and development.* Experimental & molecular medicine, 2020. **52**(5): p. 750–761.
23. Aguado, E. and M.M. Arbulo-Echevarria, *Slow phosphor-Y-LAT-ion for TCR ligand discrimination.* Nature Immunology, 2019. **20**(11): p. 1420–1422.
24. Esensten, J.H., et al., *CD28 costimulation: from mechanism to therapy.* Immunity, 2016. **44**(5): p. 973–988.
25. Chen, L. and D.B. Flies, *Molecular mechanisms of T cell co-stimulation and co-inhibition.* Nature reviews immunology, 2013. **13**(4): p. 227–242.
26. Waetzig, V. and T. Herdegen, *Context-specific inhibition of JNKs: overcoming the dilemma of protection and damage.* Trends in pharmacological sciences, 2005. **26**(9): p. 455–461.
27. Acuto, O. and F. Michel, *CD28-mediated co-stimulation: a quantitative support for TCR signalling.* Nature Reviews Immunology, 2003. **3**(12): p. 939–951.
28. Singh, R., et al., *4-1BB immunotherapy: advances and hurdles.* Experimental & Molecular Medicine, 2024. **56**(1): p. 32–39.
29. Kim, A.M.J., M.R. Nemeth, and S.-O. Lim, *4-1BB: A promising target for cancer immunotherapy.* Frontiers in Oncology, 2022. **12**: p. 968360.
30. Wang, Y.-T., et al., *Targeting 4-1BB for tumor immunotherapy from bench to bedside.* Frontiers in Immunology, 2022. **13**: p. 975926.
31. Wang, P.-Y., et al., *c-Jun enhances intestinal epithelial restitution after wounding by increasing phospholipase C-γ1 transcription.* American Journal of Physiology-Cell Physiology, 2017. **312**(4): p. C367–C375.
32. Sun, X.-M., et al., *Distinct caspase cascades are initiated in receptor-mediated and chemical-induced apoptosis.* Journal of Biological Chemistry, 1999. **274**(8): p. 5053–5060.
33. Boulares, A.H., et al., *Role of poly (ADP-ribose) polymerase (PARP) cleavage in apoptosis: caspase 3-resistant PARP mutant increases rates of apoptosis in transfected cells.* Journal of Biological Chemistry, 1999. **274**(33): p. 22932–22940.
34. Sionov, R.V., S.A. Vlahopoulos, and Z. Granot, *Regulation of Bim in health and disease.* Oncotarget, 2015. **6**(27): p. 23058.
35. O'driscoll, L., R. Linehan, and M. Clynes, *Survivin: role in normal cells and in pathological conditions.* Current cancer drug targets, 2003. **3**(2): p. 131–152.
36. Amaral, J.D., et al., *The role of p53 in apoptosis.* Discovery medicine, 2010. **9**(45): p. 145–152.
37. Urbańska, K. and A. Orzechowski, *Unappreciated role of LDHA and LDHB to control apoptosis and autophagy in tumor cells.* International journal of molecular sciences, 2019. **20**(9): p. 2085.
38. Corcoran, S.E. and L.A. O'Neill, *HIF1α and metabolic reprogramming in inflammation.* The Journal of clinical investigation, 2016. **126**(10): p. 3699–3707.

39. Thiry, A., et al., *Targeting tumor-associated carbonic anhydrase IX in cancer therapy.* Trends in pharmacological sciences, 2006. **27**(11): p. 566–573.
40. Wang, X., S. Hu, and L. Liu, *Phosphorylation and acetylation modifications of FOXO3a: Independently or synergistically?* Oncology letters, 2017. **13**(5): p. 2867–2872.
41. Heinrich, P.C., M. Müller, and L. Graeve, *Löffler/Petrides Biochemie und Pathobiochemie*. 2014: Springer-Verlag.
42. Cardenas, M.L., A. Cornish-Bowden, and T. Ureta, *Evolution and regulatory role of the hexokinases.* Biochimica et Biophysica Acta (BBA)-Molecular Cell Research, 1998. **1401**(3): p. 242–264.
43. Alves-Filho, J.C. and E.M. Pålsson-McDermott, *Pyruvate kinase M2: a potential target for regulating inflammation.* Frontiers in immunology, 2016. **7**: p. 145.
44. Wang, Q., et al., *AMPK-mediated regulation of lipid metabolism by phosphorylation.* Biological and Pharmaceutical Bulletin, 2018. **41**(7): p. 985–993.
45. Riedell, P.A., et al., *Rapcabtagene Autoleucel (YTB323) in Patients (Pts) with Relapsed/Refractory Diffuse Large B-Cell Lymphoma (R/R DLBCL): Phase II Trial Clinical Update.* Blood, 2024. **144**: p. 67.
46. Malakhova, E., et al., *Extended characterization of anti-CD19 CAR T cell products manufactured at the point of care using the CliniMACS Prodigy system: comparison of donor sources and process duration.* Cytotherapy, 2024. **26**(6): p. 567–578.
47. Prajapati, K., et al., *Functions of NKG2D in CD8+ T cells: an opportunity for immunotherapy.* Cellular & molecular immunology, 2018. **15**(5): p. 470–479.
48. Verneris, M.R., et al., *Role of NKG2D signaling in the cytotoxicity of activated and expanded CD8+ T cells.* Blood, 2004. **103**(8): p. 3065–3072.
49. Francis, N., et al., *Development of an automated manufacturing process for large-scale production of autologous T cell therapies.* Molecular Therapy Methods & Clinical Development, 2023. **31**.
50. Song, H.W., et al., *CAR-T cell expansion platforms yield distinct T cell differentiation states.* Cytotherapy, 2024. **26**(7): p. 757–768.
51. Lee, S.Y., et al., *CD8+ chimeric antigen receptor T cells manufactured in absence of CD4+ cells exhibit hypofunctional phenotype.* Journal for immunotherapy of cancer, 2023. **11**(11): p. e007803.
52. Wong, P. and E. Pamer, *Cutting edge: antigen-independent CD8 T cell proliferation.* Journal of immunology (Baltimore, Md.: 1950), 2001. **166**(10): p. 5864–5868.
53. Kaech, S.M. and R. Ahmed, *Memory CD8+ T cell differentiation: initial antigen encounter triggers a developmental program in naive cells.* Nature immunology, 2001. **2**(5): p. 415–422.
54. Iezzi, G., K. Karjalainen, and A. Lanzavecchia, *The duration of antigenic stimulation determines the fate of naive and effector T cells.* Immunity, 1998. **8**(1): p. 89–95.
55. van Stipdonk, M.J., et al., *Dynamic programming of CD8+ T lymphocyte responses.* Nature immunology, 2003. **4**(4): p. 361–365.
56. Lee, W.T., et al., *Continued antigen stimulation is not required during CD4 (+) T cell clonal expansion.* Journal of immunology (Baltimore, Md.: 1950), 2002. **168**(4): p. 1682–1689.

57. Gudmundsdottir, H., A. Wells, and L. Turka, *Dynamics and requirements of T cell clonal expansion in vivo at the single-cell level: effector function is linked to proliferative capacity.* Journal of immunology (Baltimore, Md.: 1950), 1999. **162**(9): p. 5212–5223.
58. Jelley-Gibbs, D., et al., *Two distinct stages in the transition from naive CD4 T cells to effectors, early antigen-dependent and late cytokine-driven expansion and differentiation.* Journal of immunology (Baltimore, Md.: 1950), 2000. **165**(9): p. 5017–5026.
59. Zhang, H., P. Zhao, and H. Huang, *Engineering better chimeric antigen receptor T cells.* Experimental hematology & oncology, 2020. **9**(1): p. 34.
60. Galli, E., et al., *The CD4/CD8 ratio of infused CD19-CAR-T is a prognostic factor for efficacy and toxicity.* British Journal of Haematology, 2023. **203**(4): p. 564–570.
61. Charpentier, J.C. and P.D. King, *Mechanisms and functions of endocytosis in T cells.* Cell Communication and Signaling, 2021. **19**(1): p. 92.
62. Alcover, A. and B. Alarcon, *Internalization and intracellular fate of TCR-CD3 complexes.* Critical Reviews™ in Immunology, 2000. **20**(4).
63. Valitutti, S., et al., *Degradation of T cell receptor (TCR)–CD3-ζ complexes after antigenic stimulation.* The Journal of experimental medicine, 1997. **185**(10): p. 1859–1864.
64. Miskov-Zivanov, N., et al., *The duration of T cell stimulation is a critical determinant of cell fate and plasticity.* Science signaling, 2013. **6**(300): p. ra97–ra97.
65. Love, P.E., et al., *Early events in TCR signaling–the evolving role of ITAMs.* Frontiers in Immunology, 2025. **16**: p. 1563049.
66. Zhang, W., et al., *LAT: the ZAP-70 tyrosine kinase substrate that links T cell receptor to cellular activation.* Cell, 1998. **92**(1): p. 83–92.
67. Itoh, H., et al., *Activation of immediate early gene, c-fos, and c-jun IN THE RAT SMALL INTESTINE AFTER ISCHEMIA/REPERFUSION1.* Transplantation, 2000. **69**(4): p. 598–604.
68. Barden, M., et al., *CAR and TCR form individual signaling synapses and do not cross-activate, however, can co-operate in T cell activation.* Frontiers in immunology, 2023. **14**: p. 1110482.
69. Niu, A., et al., *Differences in the phenotypes and transcriptomic signatures of chimeric antigen receptor T lymphocytes manufactured via electroporation or lentiviral transfection.* Frontiers in Immunology, 2023. **14**: p. 1068625.
70. Liu, C., et al., *Speed and location both matter: antigen stimulus dynamics controls CAR-T cell response.* Frontiers in Immunology, 2021. **12**: p. 748768.
71. Kagoya, Y., et al., *Transient stimulation expands superior antitumor T cells for adoptive therapy.* JCI insight, 2017. **2**(2): p. e89580.
72. Salter, A.I., et al., *Comparative analysis of TCR and CAR signaling informs CAR designs with superior antigen sensitivity and in vivo function.* Science signaling, 2021. **14**(697): p. eabe2606.
73. Green, D.R., N. Droin, and M. Pinkoski, *Activation-induced cell death in T cells.* Immunological reviews, 2003. **193**(1): p. 70–81.

74. Wang, R., et al., *The transcription factor Myc controls metabolic reprogramming upon T lymphocyte activation.* Immunity, 2011. **35**(6): p. 871–882.
75. Marchingo, J.M., et al., *Quantitative analysis of how Myc controls T cell proteomes and metabolic pathways during T cell activation.* elife, 2020. **9**: p. e53725.
76. Waickman, A.T. and J.D. Powell, *mTOR, metabolism, and the regulation of T-cell differentiation and function.* Immunological reviews, 2012. **249**(1): p. 43–58.
77. Pollizzi, K.N., et al., *mTORC1 and mTORC2 selectively regulate CD8+ T cell differentiation.* The Journal of clinical investigation, 2015. **125**(5): p. 2090–2108.
78. Liu, Y., et al., *Critical role of FOXO3a in carcinogenesis.* Molecular cancer, 2018. **17**(1): p. 104.
79. Chen, P.-H., et al., *Modulation of phosphoprotein activity by phosphorylation targeting chimeras (PhosTACs).* ACS Chemical Biology, 2021. **16**(12): p. 2808–2815.
80. Serrano, M.A., et al., *DNA-PK, ATM and ATR collaboratively regulate p53–RPA interaction to facilitate homologous recombination DNA repair.* Oncogene, 2013. **32**(19): p. 2452–2462.
81. Atar, D., et al., *Adapter CAR T cell therapy for the treatment of B-lineage lymphomas.* Biomedicines, 2022. **10**(10): p. 2420.

Figures

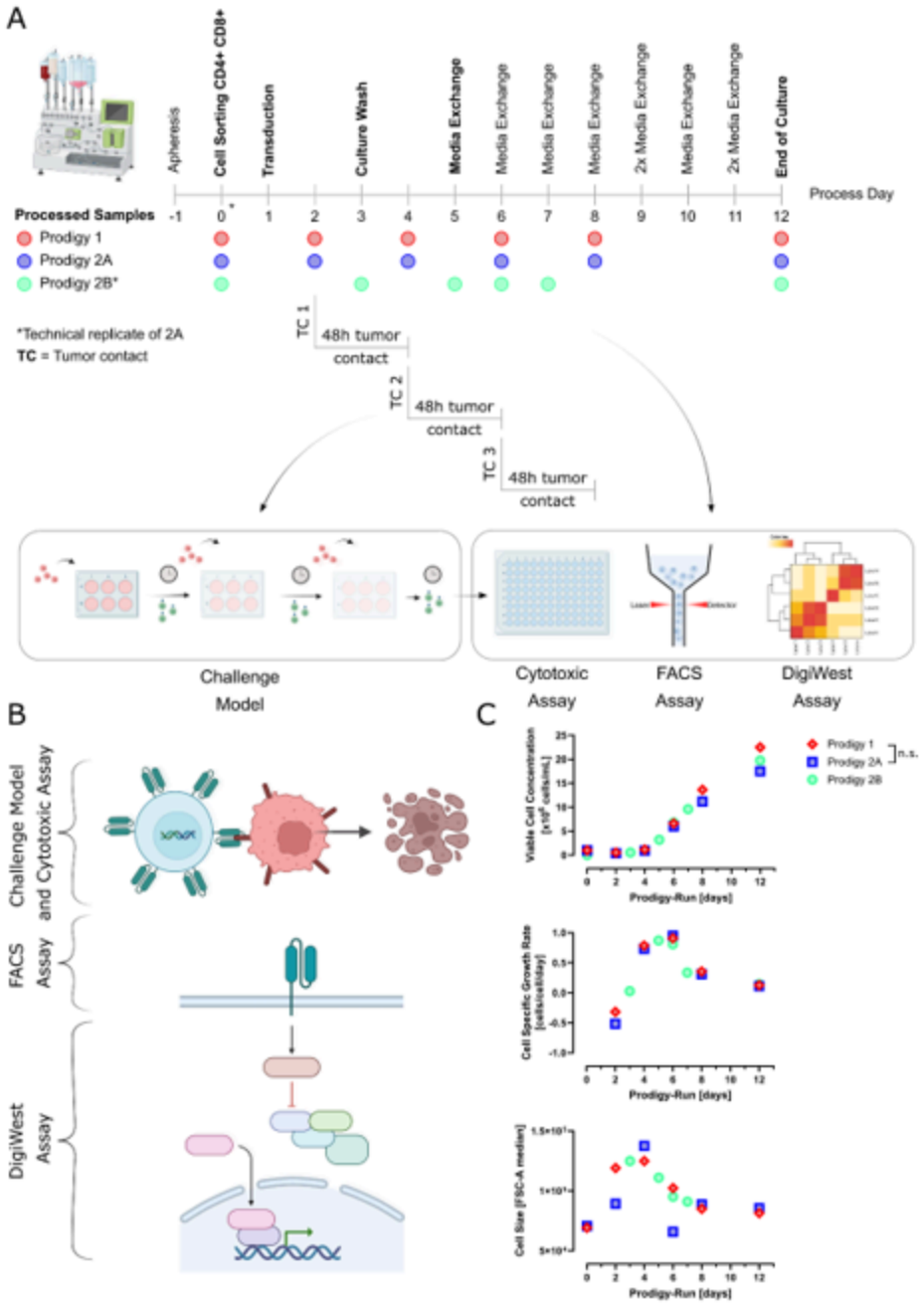


Figure 1

CliniMACS Prodigy® process run and sampling pattern for follow-up analytical procedures.

A Overview of the 12-day manufacturing process for three process runs (Prodigy 1: biological replicate no. 1, Prodigy 2: biological replicate no. 2, which branches into technical replicates Prodigy 2A and 2B). **B** Schematic interpretation of all analytical methods used to comprehensively capture the cellular phenotype. **C** Cell culture data showing total cell concentration, specific growth rate (logarithm of (current total cell count / total cell count on the previous day) / time interval between measurements)

and average cell size based on forward scatter from flow cytometry measurements. Statistical analysis indicated no significant differences (n.s.)between Prodigy 1 and Prodigy 2A, Supplementary Table 1.

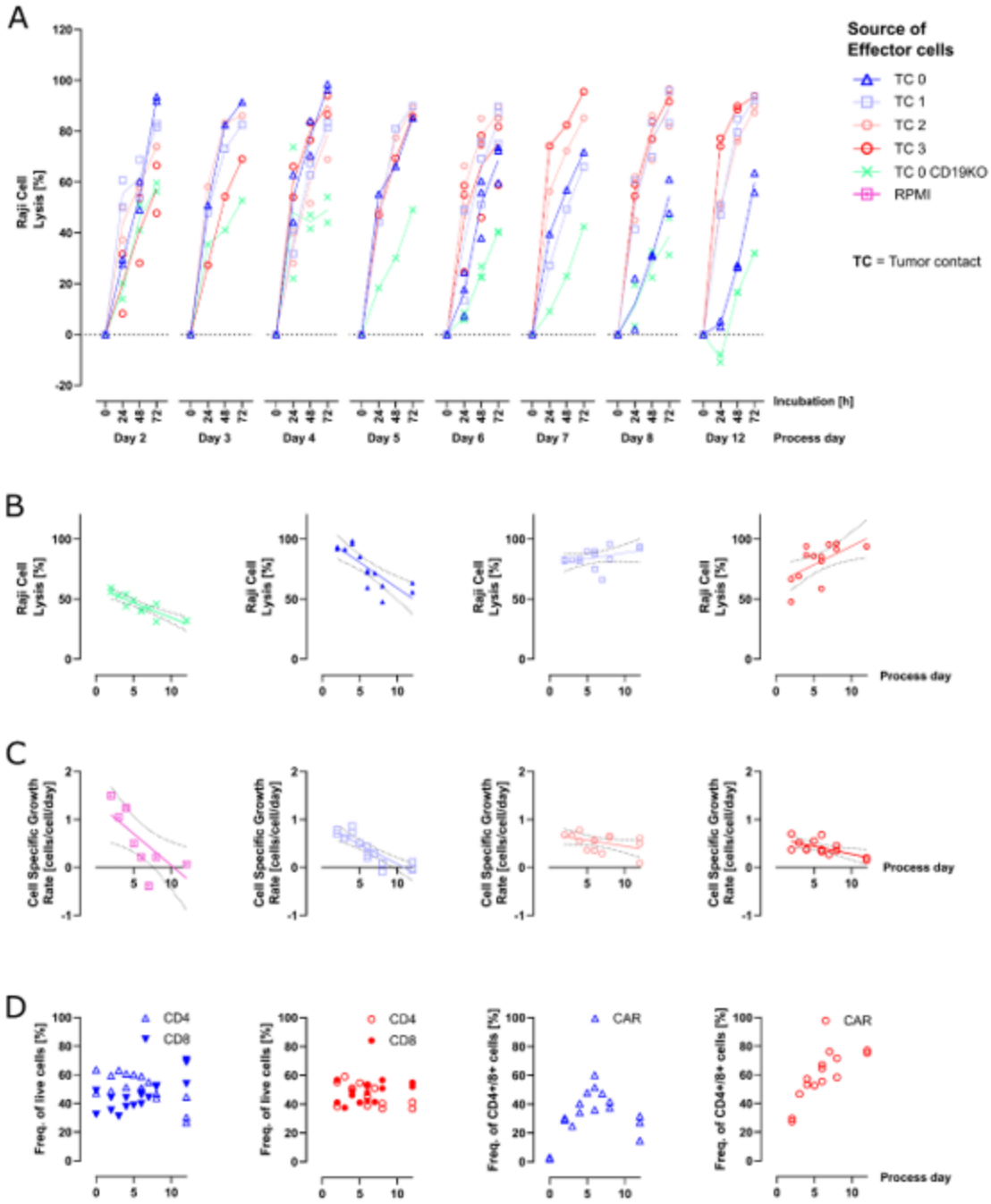


Figure 2

Functional characterization through sequential repeated tumor contacts performed on each process day.

A Cytotoxic assay plot on Raji cell lysis measured every 24 hours for each process day (lower x-axis) at an effector to target ratio of 1:1. For each sampling day, repeated tumor contacts (TC) every 48 hour were performed. TCs are shown between TC 0 (no tumor contact, sampled taken directly from

CliniMACS Prodigy®) and TC 3. Unspecific lysis measured on a CD19KO cell line of Raji (TC 0 CD19KO). Each point represents the mean of an analytical triplicate (n = 3). **B** Scatter plots for cytotoxic assay on Raji cell lysis separated for each TC. Simple linear regression was fitted independently for each group. Dotted areas indicate 95% confidence intervals. Data (except for TC 2) met the assumption of normality (Shapiro-Wilk normality test, $p > 0.05$). Slopes differed significantly from zero, $p < 0.05$ (except TC 1, $p = 0.15$). Exact slope estimates, 95% CIs, and model parameters for each group are provided in Supplementary Table 2. Significant differences based on t test between TC 0 CD19KO and TC 0 (Supplementary Table 3). **C** Scatter plots for cell specific growth rate between each TC and control (culture medium RPMI). Simple linear regression was fitted independently for each group. Dotted areas indicate 95% confidence intervals. Data met the assumption of normality (Shapiro-Wilk normality test, $p > 0.05$). Slopes differed significantly from zero, $p < 0.05$. Exact slope estimates, 95% CIs, and model parameters for each group are provided in Supplementary Table 4. **D**Scatter plots for CD4, CD8 and CD19-CAR expression.

Each point represents the mean of analytical triplicates from the biological replicates for even sample days n = 2 and one technical replicate of uneven sample days n = 1. Day 6 was sampled for all process runs. Day 12 had to be omitted for Prodigy 1.

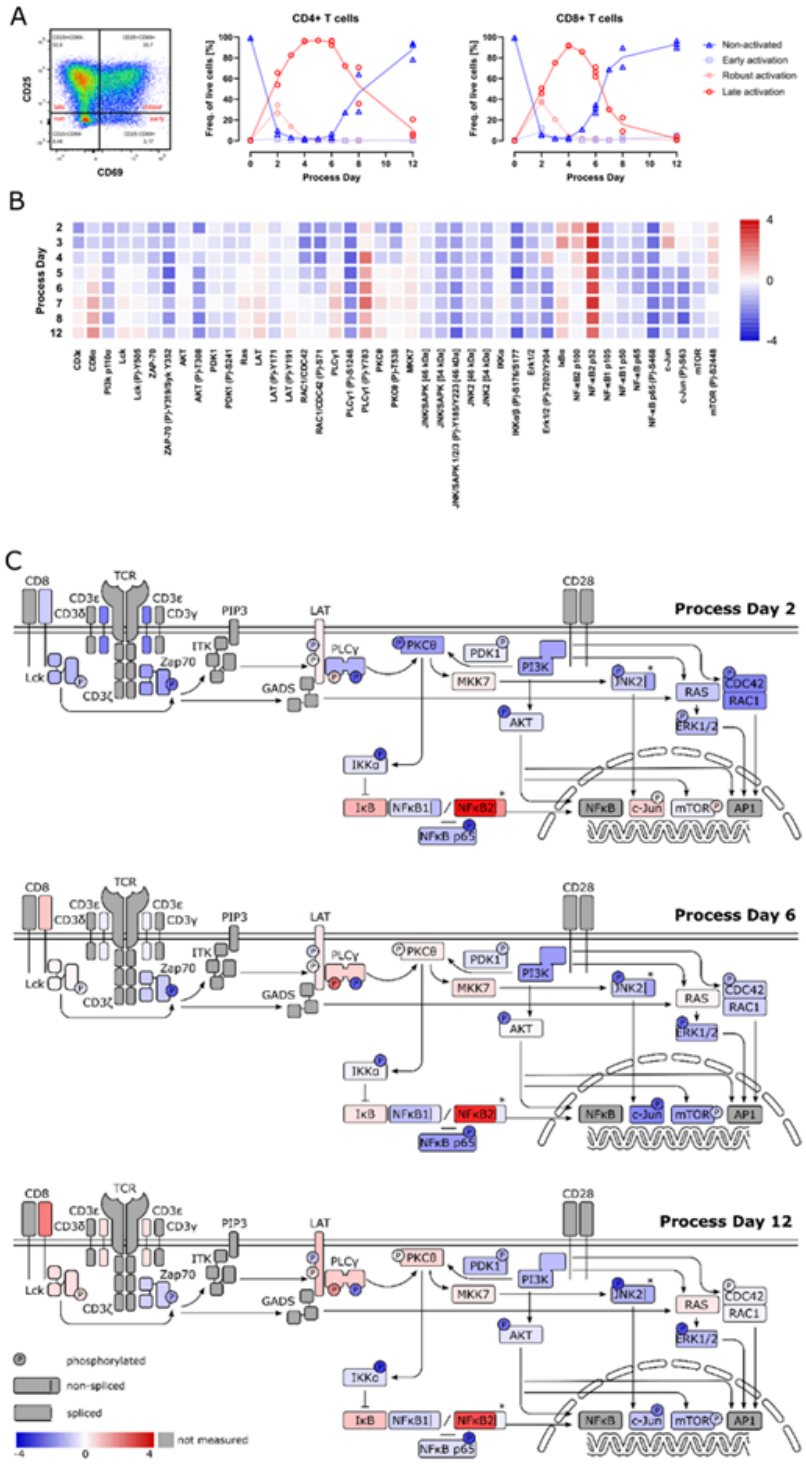


Figure 3

T cell activation profile during a 12-day CAR-T manufacturing process.

A Classification for activation state was: CD25-CD69- for non-activated, CD25-CD69+ for early-activated, CD25+CD69+ for robustly activated and CD25+CD69- for late-activate cells. Samples are shown before first tumor contact (TC 0). Each point represents the biological replicates for even sample days (n = 2)

and one technical replicate of uneven sample days (n = 1). **B** Heat map of expression signals for each analyte detected via DigiWest™ technology. Phosphorylation of proteins indicated by (P), followed by its respective residue. Data was median centered and log-2 transformed to the respective day 0 signal of each analyte. Samples are shown for Prodigy 2 (n = 1) and its technical replicate (n = 1), mean values represented for day 6 and 12 (n = 2). Data of Prodigy 1 can be found in Supplementary Figure 3. **C** T-cell activation signaling cascade [20-27] with each node color-coded to reflect corresponding DigiWest™ median centered and log-2 transformed data. Data shown for Prodigy 2A.

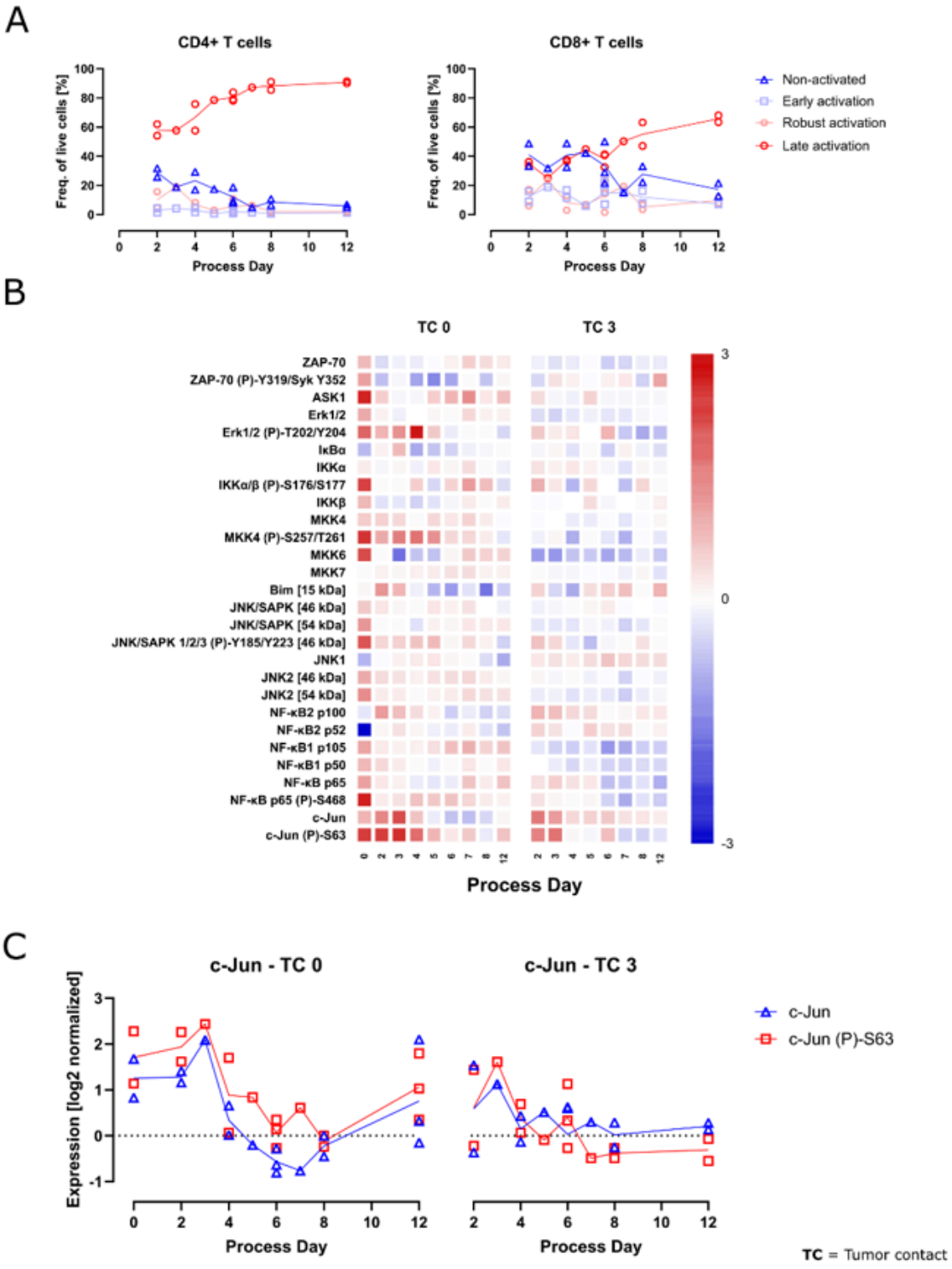


Figure 4

Activation and CAR-signaling dynamics before and after tumor engagement.

A Flow cytometry-based scatter plot of activation profile. Classification for activation state was: CD25-CD69- for non-activated, CD25-CD69+ for early-activated, CD25+CD69+ for robustly activated and CD25+CD69- for late-activate cells. Samples taken after three consecutive tumor contacts (TC 3). Each point represents the biological replicates for even sample days (n = 2) and one technical replicate of uneven sample days (n = 1). Day 6 was sampled for all process runs (n = 3). Process day 12 sample of Prodigy 1 had to be omitted for TC 3 (n = 2). **B** Heat map of expression signals for each analyte detected via DigiWest™ technology. Phosphorylation for analytes indicated by (P) followed by its respective residue. Data was median centered and log-2 transformed, separately for samples of Prodigy 1 or Prodigy 2. Data are shown for Prodigy 2A, for even sample days (n = 1) and Prodigy 2B for uneven sample days (n = 1). Day 6 and 12 were sampled for both process runs, mean values represented (n = 2). Data of Prodigy 1 can be found in Supplementary Figure 5. **C** Scatter plot of DigiWest™ data for c-Jun (TC 0) and after tumor contact (TC 3). Each point represents the biological replicates for even sample days n = 2 and one technical replicate of uneven sample days n = 1. Day 6 was sampled for all process runs (n = 3). **D** CAR-signaling cascade [28-30], with each node color-coded to reflect corresponding DigiWest™ data expression levels. Data shown for Prodigy 2B (n = 1).

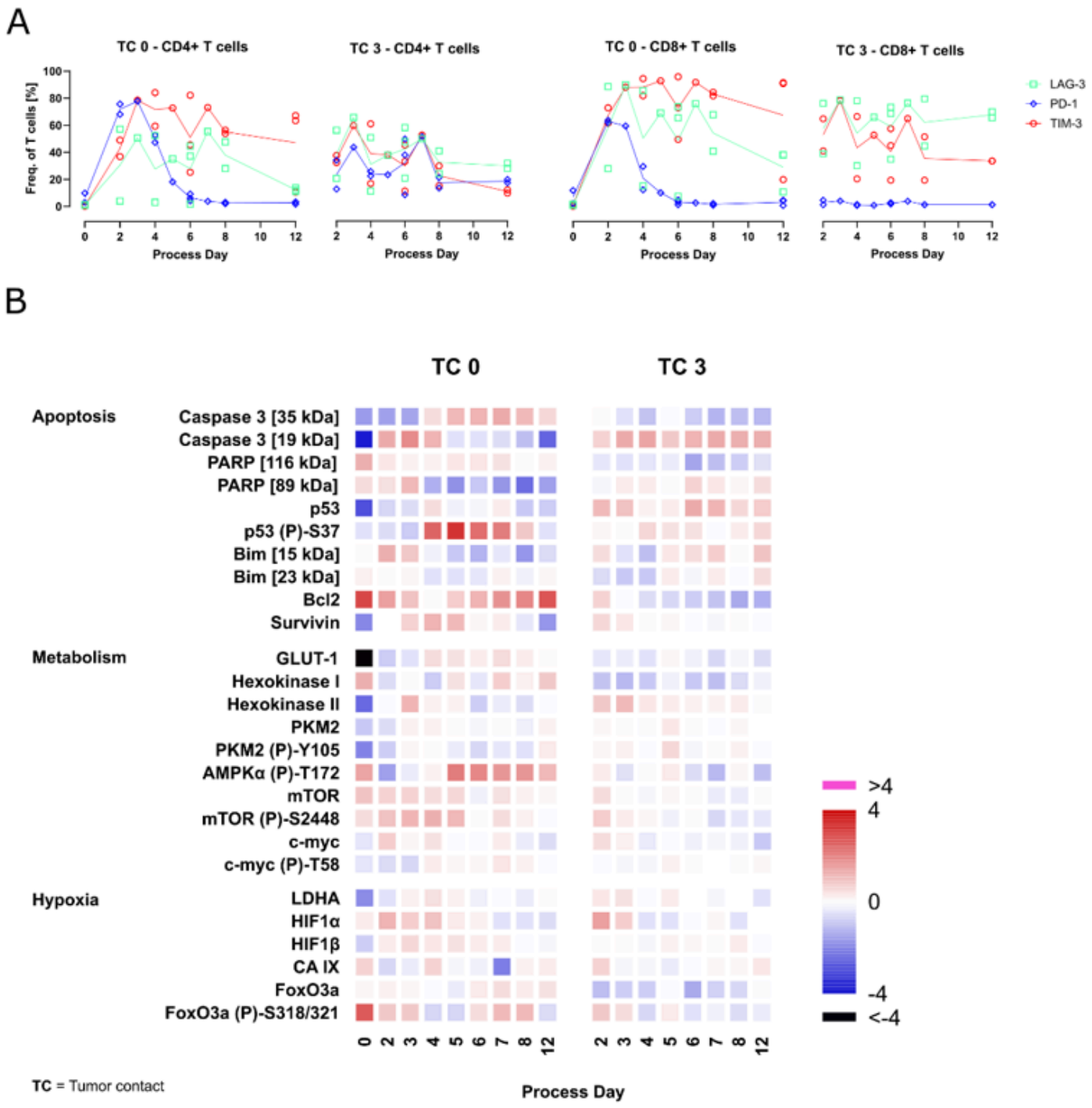


Figure 5

Expression profiles of inhibitory immune checkpoints, metabolism, hypoxia, and apoptosis.

A Flow cytometry-based scatter plot of markers for inhibitory immune checkpoints LAG-3, PD-1 and TIM-3. Samples taken before tumor contact (TC 0) and after three consecutive tumor contacts (TC 3). Each point represents the biological replicates for even sample days (n = 1) and one technical replicate of uneven sample days (n = 1). Day 6 was sampled for all process runs (n = 3). Process day 12 sample of Prodigy 1 had to be omitted for TC 3 (n = 2). **B** Heat map of expression signals for each analyte detected

via DigiWest™ technology. Phosphorylation for analytes indicated by (P) followed by its respective residue. Data was median centered and log-2 transformed, separately for samples of Prodigy 1 or Prodigy 2. Data are shown for Prodigy 2A, for even sample days (n = 1) and Prodigy 2B for uneven sample days (n = 1). Day 6 and 12 were sampled for both process runs, mean values represented (n = 2). Data of Prodigy 1 can be found in Supplementary Figure 6.

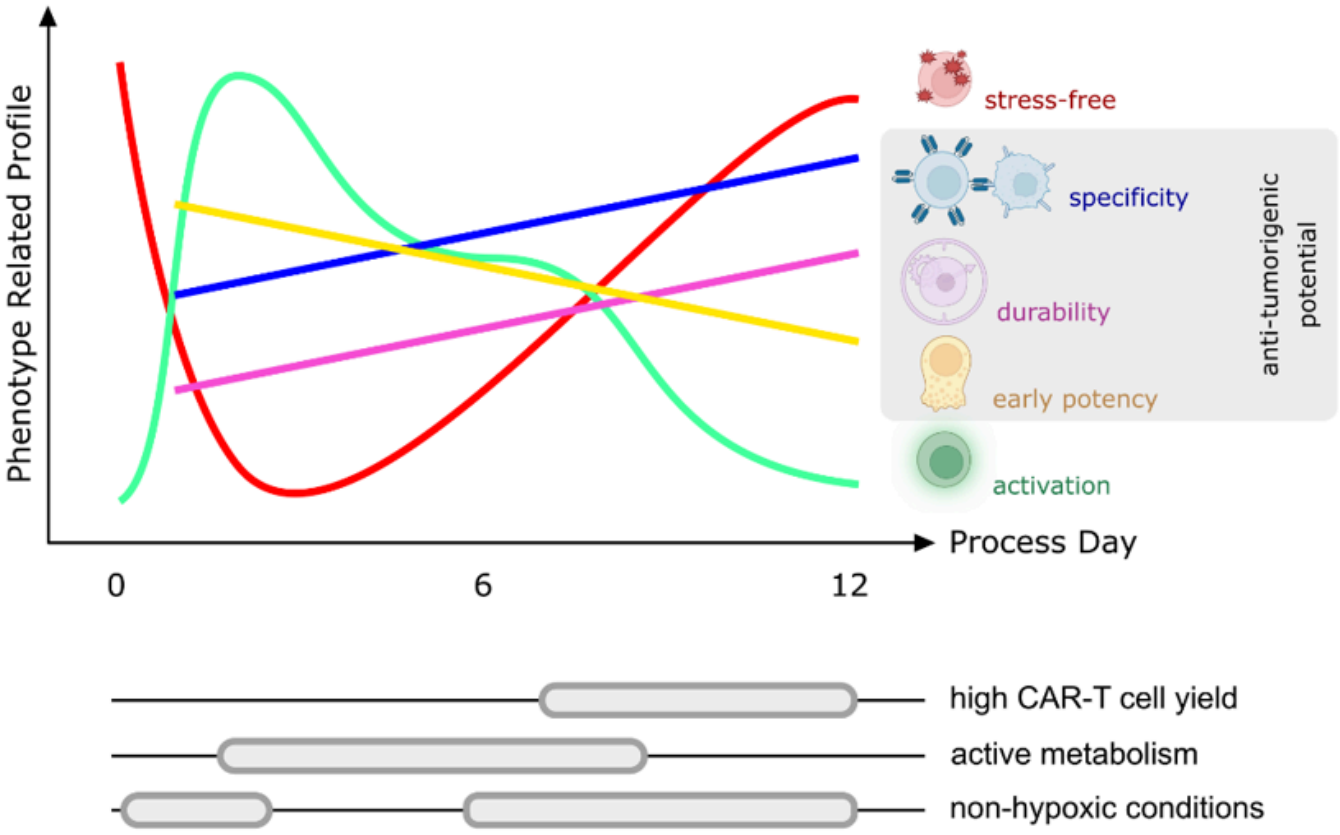


Figure 6

Process characterisation and phase-specific profiling

Approximation of the 12-day-cellular stress response profile, target specificity, cytotoxic durability (post three tumor contacts), early cytolytic potency upon initial tumor engagement and T cell activation dynamics. Additionally, process-related metrics including CAR-T cell yield, metabolic reprogramming and adaption to hypoxic conditions.

Supplementary Files

This is a list of supplementary files associated with this preprint. Click to download.

- Supplementary.docx